Metal-insulator and magnetic phase diagram of Ca_2RuO_4 from auxiliary field quantum Monte Carlo and dynamical mean field theory

Hongxia Hao,[1] Antoine Georges,[2,3,4,5] Andrew J. Millis,[3,6] Brenda Rubenstein,[1] Qiang Han,[6] and Hao Shi[3,*]

[1]*Department of Chemistry, Brown University, Providence, Rhode Island 02912, USA*
[2]*Collège de France, 11 Place Marcelin Berthelot, 75005 Paris, France*
[3]*Center for Computational Quantum Physics, Flatiron Institute, New York, New York 10010, USA*
[4]*CPHT, CNRS, École Polytechnique, IP Paris, F-91128 Palaiseau, France*
[5]*DQMP, Université de Genève, 24 quai Ernest Ansermet, CH-1211 Genève, Suisse*
[6]*Department of Physics, Columbia University, New York, New York 10027, USA*

(Received 11 November 2019; accepted 1 May 2020; published 2 June 2020)

Layered perovskite ruthenium oxides exhibit a striking series of metal-insulator and magnetic-nonmagnetic phase transitions easily tuned by temperature, pressure, epitaxy, and nonlinear drive. In this work, we combine results from two complementary state-of-the-art many-body methods, auxiliary field quantum Monte Carlo and dynamical mean field theory, to determine the low-temperature phase diagram of Ca_2RuO_4. Both methods predict a low-temperature, pressure-driven metal-insulator transition accompanied by a ferromagnetic-antiferromagnetic transition. The properties of the ferromagnetic state vary nonmonotonically with pressure and are dominated by the ruthenium d_{xy} orbital, while the properties of the antiferromagnetic state are dominated by the d_{xz} and d_{yz} orbitals. Differences in the details of the predictions of the two methods are analyzed. This work is theoretically important as it presents the first application of the auxiliary field quantum Monte Carlo method to an orbitally degenerate system with both Mott and Hunds physics and provides an important comparison of the dynamical mean field and auxiliary field quantum Monte Carlo methods.

DOI: 10.1103/PhysRevB.101.235110

I. INTRODUCTION

The quantum many-body problem is one of the grand challenge scientific problems of our time [1]. Recent work [2–4] suggests that an important route towards a solution is to attack important problems via complementary methods. In this paper, we use the auxiliary field quantum Monte Carlo (AFQMC) and dynamical mean field theory (DMFT) methods to study the low-temperature phase diagram and physical properties of Ca_2RuO_4. In the form used in this article, AFQMC is a zero-temperature, finite-system method that employs an imaginary-time projection which samples the space of non-orthogonal Slater determinants to estimate the ground-state wave function [5,6]. In contrast, DMFT uses a self-energy locality assumption to approximate Green's functions at nonzero temperature [7]. The completely different natures of the approximations made and computational challenges faced by the two methods mean that a comparison of results yields important insights into both the actual physics of the systems studied and the validity of the different approximations.

The material chosen for study, Ca_2RuO_4 (Fig. 1), is a member of a fascinating and extensively studied family of ruthenium-based compounds with chemical formulas $Sr_{n+1}Ru_nO_{3n+1}$ and $Ca_{n+1}Ru_nO_{3n+1}$. This family of materials has been of intense interest for their remarkable properties, including their unconventional superconductivity [8], variety of magnetic phases [9,10], nematicity metal-insulator transitions [11,12], and unusual nonequilibrium properties [13], all of which are believed to be due to strong Hubbard and Hunds electron-electron interactions among the electrons in the Ru-derived t_{2g} orbitals [14].

Ca_2RuO_4 forms a Pbca symmetry structure derived from the $n = 1$ Ruddlesden-Popper structure by rotations and tilts of the RuO_6 octahedra. The unit cell contains four Ru ions, equivalent up to a translation and rotation of the RuO_6 octahedron. At ambient pressure, the material undergoes a metal-insulator transition as the temperature is decreased below ∼350 K and becomes antiferromagnetic below ∼110 K [9,15–17]. Increasing pressure decreases the metal-insulator transition temperature [11,12], with the system remaining metallic at room temperature at pressures above ∼0.5 GPa [11,12] and down to very low temperatures for $P > 2$ GPa [18]. Low-T ferromagnetism is reported for pressures of several GPa, with T_c varying from 10 to 30 K [18]. The material may exist in two closely related forms: S-Pbca (for short) and L-Pbca (for long), distinguished by whether the apical Ru-O bond length and c-axis lattice parameter are relatively longer (L) or shorter (S). The S-Pbca structure is associated with insulating and antiferromagnetic (AFM) behavior, and the L-Pbca structure with metallic and ferromagnetic (FM) behavior. Capturing the interplay between structural and electronic properties is an important challenge for theory.

Previous publications have studied Ca_2RuO_4 using density functional theory (DFT) and its "$+U$" [19,20] and plus

*hshi@flatironinstitute.org

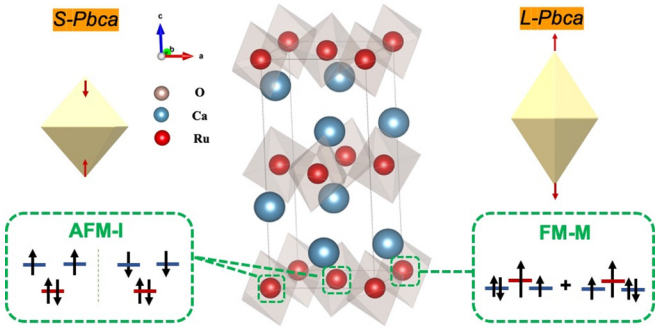

FIG. 1. Crystal structure of Ca_2RuO_4 (central portion), with calcium shown in blue, oxygen in gray, and ruthenium in red. The primitive vectors $\vec{a}$, $\vec{b}$, and $\vec{c}$ are defined using the orthorhombic convention. Left side: Depiction of the short-bond RuO_6 octahedron occurring in the low-T, ambient-pressure S-Pbca structure (top) with a depiction of the dominant Ru multiplet term in the local electronic structure of the insulating state beneath. The d_{xy} orbital (red bar) is fully occupied and the xz/yz orbitals (blue bars) are half-filled and in a high-spin state. Right side: Depiction of the long-bond RuO_6 octahedron occurring in the high-T or high-P L-Pbca structures (top), with a depiction of the dominant Ru multiplet term in the ferromagnetic state beneath. A nearly half-filled, spin-polarized xy orbital (red bar) with the remaining hole is in a superposition of xz/yz states (blue bars).

dynamical mean field theory (DFT + DMFT) [21–24] extensions. However, these works primarily focused on ambient pressure phases and have each presented results from only one theoretical method. Further, $+U$ methods treat the many-body physics via a Hartree-type approximation, while DMFT, which transcends static mean field theory, makes a strong self-energy locality assumption that may be questioned for electronically two-dimensional materials such as the ruthenates. For this reason, cross-comparison with another many-body method, such as AFQMC method considered here, is invaluable.

The remainder of the paper is organized as follows. In Sec. II, we outline the model and structural conditions and adapt them to the AFQMC and DMFT methods. In Sec. III, we present systematic results regarding the metal-insulator and magnetic phase transition between the two methodologies and demonstrate the substantially similar results for the nature of the electronic and physical properties. We conclude with a discussion of this work and its potential applications to the strongly correlated systems in Sec. IV.

II. MODEL AND METHODOLOGY

We downfold the full electronic structure of Ca_2RuO_4 to a material-based, three-band Hamiltonian representing the correlated frontier orbitals for several different crystal structures by first using the non-spin-polarized generalized gradient approximation (GGA) [25–28] to obtain an electronic band structure. We then extract frontier orbitals near the Fermi-surface states from the GGA calculations via a maximally localized Wannier function construction as implemented in Wannier90 [29,30]. The GGA calculations are performed using experimentally determined atom positions obtained from ambient-pressure studies performed at room temperature and $T = 400$ K [15,17], as well as room-temperature studies performed at pressures of 1–5 GPa [12]. For simplicity, we denote the experimentally determined structures as S-295 K for the structure at 295 K, ambient pressure (S-Pbca symmetry), and L-5GPa for the structure at 295 K, 5GPa (L-Pbca symmetry). For all of the other experimentally determined geometries we study in the paper, we use L-400K for the structure at 400 K, ambient pressure (L-Pbca symmetry); L-1GPa for the structure at 295 K, 1 GPa (L-Pbca symmetry); and L-3GPa for the structure at 295 K, 3 GPa (L-Pbca symmetry). Local Coulomb "U" and "J" interaction terms are then added, with $U = 2.3$ eV and $J = 0.35$ eV, parameters previously found to produce reliable representations of the properties and phase diagrams of perovskites including $CaRuO_3$, $SrRuO_3$, and $BaRuO_3$ [31–33], as well as Sr_2RuO_4 [34] (see also Ref. [35] for a direct determination of the Hund's coupling from photoemission measurements on Ca_2RuO_4). The resulting low-energy theory is a three-band Hubbard-Kanamori Hamiltonian [36,37]:

$$\begin{aligned}\hat{H} = &\sum_{ij\nu\nu'\sigma} t_{ij}^{\nu\nu'} \hat{c}_{i\nu\sigma}^{\dagger} \hat{c}_{j\nu'\sigma} + U \sum_{i\nu} \hat{n}_{i\nu\uparrow}\hat{n}_{i\nu\downarrow} \\ &+ \sum_{i,\,\nu\neq\nu',\,\sigma\sigma'} (U - 2J - J\delta_{\sigma\sigma'})\hat{n}_{i\nu\sigma}\hat{n}_{i\nu'\sigma'} \\ &+ J \sum_{i,\,\nu\neq\nu'} (\hat{c}_{i\nu\uparrow}^{\dagger}\hat{c}_{i\nu'\downarrow}^{\dagger}\hat{c}_{i\nu\downarrow}\hat{c}_{i\nu'\uparrow} + \hat{c}_{i\nu\uparrow}^{\dagger}\hat{c}_{i\nu\downarrow}^{\dagger}\hat{c}_{i\nu'\downarrow}\hat{c}_{i\nu'\uparrow}). \quad (1)\end{aligned}$$

In the above, $\hat{c}_{i\nu\sigma}^{\dagger}$ creates an electron with spin σ in Wannier state ν at lattice site i and $\hat{n}_{i\nu\sigma}$ denotes the corresponding number operator. The index ν labels states derived from the Ru t_{2g}-symmetry d orbitals (with the appropriate admixture of oxygen wave functions). The first term in the Hamiltonian describes the near-Fermi-surface band structure, the second describes the intraorbital Coulomb repulsion, the third describes the interorbital Coulomb repulsion, and the last contains the electron pair-hopping and exchange contributions. The *ab initio* parameters, $t_{ij}^{\nu\nu'}$, are obtained from a Wannier analysis. (See Ref. [38], Sec. I, for more details about the one-body matrix and its raw data.) The on-site $i = j$ term is a 3×3 matrix parametrizing the energy splitting between the different t_{2g}-symmetry d orbitals. In a basis aligned with the local RuO_6 octahedron, $t_{i=j}$ is diagonal, with two degenerate eigenvalues giving the on-site energy of the $d_{xz/yz}$ orbitals and a third eigenvalue giving the energy of the d_{xy} orbital. The crystal-field level splitting, $\Delta = \epsilon_{yz} - \epsilon_{xy}$, is generally larger in the S-Pbca structure than in L-Pbca structures. For example, $\Delta = 0.23$ eV for the ambient-pressure, 295 K S-Pbca structure, while $\Delta = 0.10$ eV for the ambient-pressure, 400 K L-Pbca structure. As pressure is applied, the crystal-field splitting decreases to $\Delta = 0.06$ eV for the L-1GPa structure and even to a negative value of $\Delta = -0.02$ eV for the L-5GPa structure. It is important to emphasize that Δ is a "bare" parameter, which is small compared to the bandwidths but whose effects may be strongly enhanced by correlations.

We treat the interactions using the AFQMC and DMFT methods. Extending the AFQMC methodology, which has heretofore mainly been applied to variants of the single-orbital Hubbard model, to the multiband, Hunds metal case

has been an important challenge. Here, we employ the methods introduced in Ref. [36] to overcome this challenge. In AFQMC, one typically studies three-dimensional $L_x \times L_y \times L_z$ supercells. We have found that correlations along z are typically very weak and therefore set $L_z = 1$ for most of the calculations. A $1 \times 1 \times 1$ unit cell contains 4 Ru ions; the largest cell we study is $4 \times 4 \times 1$, containing 64 Ru ions. The AFQMC method uses imaginary-time propagation of a trial wave function to converge to a ground state. Our calculations use different types of trial wave functions including free-electron, as well as AFM and FM Hartree-Fock states. The self-consistent procedure in Ref. [39] is applied to find the best single-determinant trial wave function. (See Ref. [38], Sec. II A, for more details about the preparation of our trial wave functions.)

We solve the three-band model employing the single-shot (no charge self-consistency) DMFT [22,24,31–33] approximation, which treats the experimental crystal structure and uses the hybridization expansion variant of the continuous-time quantum Monte Carlo (CT-HYB) solver as implemented in the Toolbox for Research on Interacting Quantum Systems (TRIQS) library [40,41]. Within our DMFT calculations, the single-site approximation is made and the orbital basis at each of the four crystallographically inequivalent Ru sites is aligned with the local octahedral axes to minimize the sign problem.

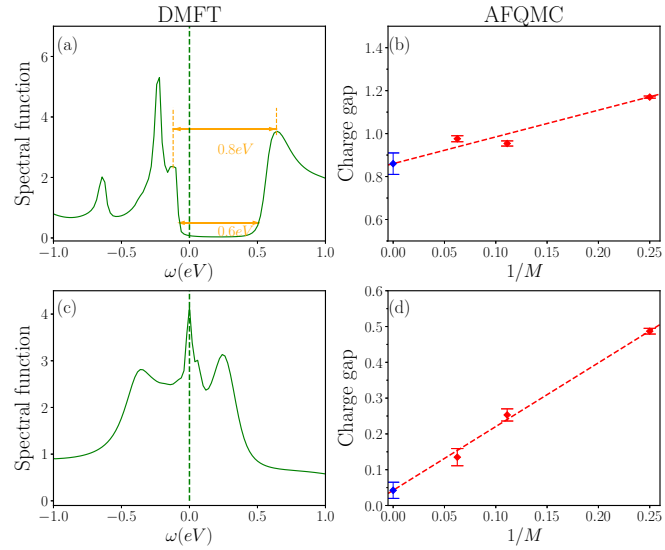

FIG. 2. Comparison of the charge gap predictions from DMFT and AFQMC for the L-Pbca and S-Pbca structures. DMFT results are calculated at 60 K and AFQMC results are calculated at 0 K. Left: Spectral functions per Ru obtained using DMFT simulations with analytical continuation for the S-295K structure (a) and L-5GPa structure (c). Right: Extrapolation of the charge gap to the thermodynamic limit in AFQMC calculations of the S-295K structure (b) and L-5GPa structure (d). In (b) and (d), the M on the x axis represents the number of unit cells used in the AFQMC simulations.

III. RESULTS AND DISCUSSION

We now present our results, beginning with the ambient-pressure, low-T S-Pbca structure. In this structure, Ca_2RuO_4 is an antiferromagnetic insulator (AFM-I) with an essentially fully occupied d_{xy} orbital and half-filled $d_{xz/yz}$ orbitals [22,35]. The half-filled orbitals are in a high-spin configuration and the Ru sites are antiferromagnetically ordered below a Néel temperature of approximately 110 K. Our calculations reproduce the observed insulating, AFM ground state. Our AFQMC simulations are for finite-sized systems and have no spontaneous symmetry breaking, but calculations of the spin-spin correlation function reveal that the spatial extent of the correlations is at least the size of the computational system. Our DMFT calculations were conducted at 60 K and recover a fully polarized AFM state and a very low imaginary self-energy. The upper panels in Fig. 2 present the gap to charge excitations computed in both methods. The left panel shows the many-body density of states computed within DMFT for the ambient pressure, $T = 295$ K structure using maximum-entropy analytical continuation of imaginary-time quantum Monte Carlo measurements of the Green's function. The right panel shows the AFQMC charge gap computed from the difference of ground-state energies having different particle numbers: $\Delta_g = E_{N-1} + E_{N-1} - 2E_N$. The charge gap was calculated for $2 \times 2 \times 1$, $3 \times 3 \times 1$, and $4 \times 4 \times 1$ supercells (note that the $1 \times 1 \times 1$ unit cell was not included in our extrapolation due to its finite-size effects (See Ref. [38], Sec. II B, for further details regarding our extrapolations.), and linear extrapolation was performed with respect to the inverse of the total number of unit cells in the computational system, revealing an $M \to \infty$ charge gap that is ∼0.8 eV. This is larger than the 0.6-eV DMFT charge gap but consistent with the energy separation between the density-of-states maxima seen in the DMFT calculations. Within the DMFT calculations, the physics of the insulating state is evident: from the orbitally resolved density of states (for details see Ref. [38], Figs. 3 and 4 and Table III), one sees a fully occupied xy band and half-occupied xz/yz states with clear upper and lower Hubbard band structure. The near-quantitative agreement between the two calculations is strong evidence that both methods correctly represent the insulating AFM state. The reported experimental optical gap in the AFM phase is of the order of 0.6–0.7 eV [20].

We next turn to the 5GPa L-Pbca structure, experimentally known to host a metallic state with a ferromagnetic transition at temperatures below 10 K [18]. For this structure, both our DMFT and our AFQMC calculations uncover a ferromagnetic metal (FM-M). The DMFT Néel temperature of roughly 70 K is determined by applying a magnetic field H, computing the resulting magnetization, and plotting the data according to the Arrott relation, $m^2 = c_1 H/m - c_2(T - T_c)$. Note that, because DMFT neglects spatial fluctuations, it is expected to overestimate the ordering temperature. In order to determine the ground state magnetic order in AFQMC, we break the spin symmetry of the AFQMC trial wave function and compare the QMC energies of the different symmetry sectors. The DMFT density of states is shown in the lower-left panel in Fig. 2 and is clearly metallic. The extrapolated gap based on the AFQMC calculations is shown in the lower-right panel and, again, is consistent with a metallic state. We rationalize the appearance of the metallic state by noting that the increased pressure decreases the crystal field splitting, thereby promoting the transfer of electrons from the d_{xy} to the $d_{xz/yz}$

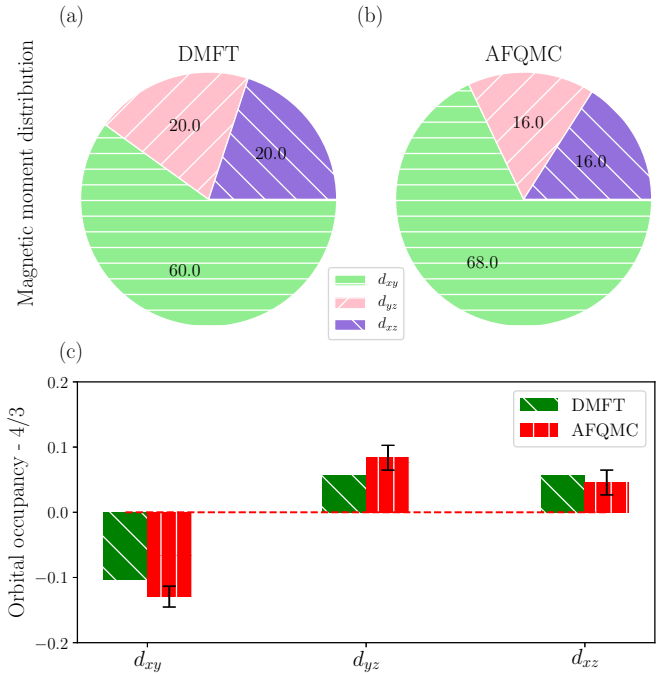

FIG. 3. Comparison of magnetic moment distributions and orbital occupancies obtained by DMFT at 60 K and AFQMC at 0 K for the experimentally acquired L-Pbca L-5GPa structure. (a) Magnetic moment distributions from DMFT: 60% of the magnetic moment is in the d_{xy} band. (b) Magnetic moment distributions from AFQMC: 68% of the magnetic moment is in the d_{xy} band. (c) Orbital occupancies from DMFT and AFQMC: the y axis is shifted by an average density of 4/3. A smaller d_{xy} band occupancy results from a negative crystal field splitting.

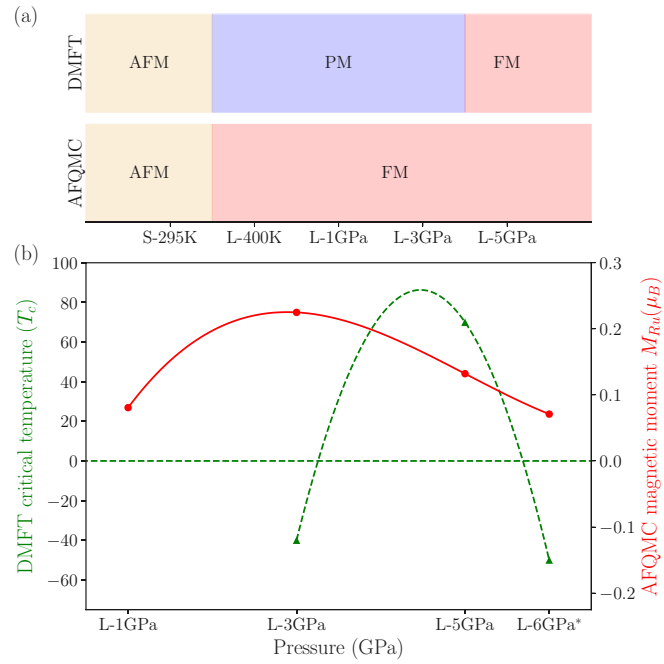

FIG. 4. (a) Phase diagram of Ca_2RuO_4 for different lattice structures. Both DMFT and AFQMC predict the S-295K structure to be an AFM-I and the L-5GPa structure to be an FM-M. At intermediate pressures, both DMFT and AFQMC find Ca_2RuO_4 to be a metal, but AFQMC predicts an FM-M state, while DMFT predicts a paramagnetic metal (PM-M) state (based on the range of temperatures we could access). (b) The red line depicts the ground-state magnetic moments obtained using AFQMC as a function of the pressure. The green line is a guide for the eye that denotes the critical temperature obtained as a function of the pressure with DMFT. Pressures at which there is no FM order are depicted as having negative critical temperatures. Note that the structure at $P = 6$ GPa shown in (b) is obtained by linear extrapolation of experimentally determined atom positions at $P = 1$ GPa and $P = 3$ GPa. (See Ref. [38], Sec. III B, for details regarding the interpolations).

orbitals. The lower panels in Fig. 3 show the deviations of orbital occupancy from the equal occupancy value of $\frac{4}{3}$ for different structures; the two methods agree very well. The relatively small changes in crystal field splitting are enhanced by interaction effects, leading to almost equally occupied orbitals in the L-Pbca structure and fully occupied d_{xy} orbitals in the S-Pbca structure.

To further characterize the metallic, magnetic state, we present in the upper panels in Fig. 3 the orbital content of the magnetic moments determined from DMFT and AFQMC calculations of the L-Pbca ferromagnetic state. The two methods agree that, despite the nearly equal occupancies of the three orbitals, the dominant contribution to the ferromagnetism comes from the d_{xy} orbital. The enhanced contribution of the xy orbital to the magnetic moment may arise from the strong van Hove singularity occurring near the Fermi surface in the d_{xy} density of states.

The ground-state phase diagram of Ca_2RuO_4 at various pressures is depicted in Fig. 4. Both AFQMC and DMFT find the S-Pbca, S-295K structure to be an AFM-I, consistent with experimental findings [15,17]. Both methods also find all of the L-Pbca structures studied, including the L-400K, L-1GPa, L-3GPa, and L-5GPa structures, to possess a metallic ground state and the L-5GPa structure to be in the FM-M state. However, AFQMC and DMFT predict different magnetic properties for many of the L-Pbca structures. For the L-400K, L-1GPa, and L-3GPa structures, AFQMC finds an FM-M state, while DMFT finds a PM-M state. Note, however, that this conclusion relies on an extrapolation from the lowest temperature that we could study (60 K). It will be interesting in the future to reconsider this extrapolation as improved DMFT solvers [42] able to reach much lower temperatures become available. Interestingly, Ca_2RuO_4 was found to be in a mixed AFM-FM state at pressures of less than 3 GPa [43]. For pressures above 5 GPa, experiments find FM order, but the critical temperature exhibits a nonmonotonic behavior with pressure and peaks between 3 and 5 GPa in experiments [18]. We plot the critical temperature from DMFT (obtained from Arrott plots; see Ref. [38], Sec. III C, for details.) as a function of the pressure in Fig. 4(b). A dome-shaped curve of critical temperature vs pressure is observed, with a peak around 5 GPa. We depict the critical temperature as being negative when DMFT does not recover an FM state. While the AFQMC ground state is always ferromagnetic, magnetic moments also exhibit a nonmonotonic behavior, which indicates that FM order is favored at intermediate pressures. The maximum critical temperature indicated by the magnetic

moment is shifted to lower pressures in AFQMC, with its peak instead occurring around 3 GPa.

IV. SUMMARY

In summary, we have employed two state-of-the-art electronic structure methods—a new implementation of AFQMC suitable for multiorbital and Hunds-coupled models, and DMFT—to study Ca_2RuO_4's phase diagram and physical properties as a function of the pressure. Our calculations are based on a model Hamiltonian with bare electronic parameters taken from Wannier fits to density functional calculations for different experimentally reported structures. We find that the two theoretical methods yield substantially similar results for the nature of the electronic state (metal vs insulating) and basic electronic properties including gaps and the orbital content of magnetic moments. As noted in previous work [21–24,35], the key to the physics is the enhancement, by interactions, of structurally induced differences in the on-site splitting between the different electronic states, which, although small in comparison to the overall bandwidths, drive substantial differences in the occupancies of its t_{2g} orbitals.

The agreement between methods, occurring despite their very different approximations and sources of errors, adds confidence both to the methods and to the emerging physical picture. The most significant discrepancy between the methods is the different magnetic phase diagram for the high-pressure phases of Ca_2RuO_4's magnetic ordering between 1 and 5 GPa. The two methods agree on the qualitative features including the presence of a dome of magnetization, with the strongest magnetic state occurring at an intermediate pressure, but disagree on the exact range of pressures where magnetism is observed and on the pressure that maximizes the tendency toward magnetism. The difference may be due to intersite effects requiring a cluster dynamical mean field treatment in this quasi-two-dimensional system, limitations in extrapolating DMFT results down to very low temperatures (calling for the development of improved solvers), or bias in AFQMC from the choice of initial wave function or the constrained path approximation.

Our work suggests several interesting extensions. The methodology employed here is directly applicable to $Ca_{2-x}Sr_xRuO_4$ materials, strontium-doped versions of Ca_2RuO_4 that interpolate between the AFM-I Ca_2RuO_4 studied here and metallic and superconducting Sr_2RuO_4 [8]. Past works have shown that increasing x is analogous to increasing the temperature or pressure in this work, leading to the evolution of a metal for large values of x [17,44]. Nevertheless, $Ca_{2-x}Sr_xRuO_4$ exhibits a number of yet-to-be-explained exotic phases, including a metamagnetic phase that emerges for $0.2 < x < 0.5$ [44]. Beyond these specific applications, the methodologies employed here are ripe for application to the many $4d$- and $5d$-transition metal oxides whose complex interplay of spin-orbit coupling, exchange, and crystal field effects have and continue to reveal unexpected physics. Most importantly, despite their algorithmic limitations, our new multiband AFQMC methodology and DMFT predict similar insulating and magnetic orders over wide swaths of Ca_2RuO_4's phase diagram, differing only in their predictions of Ca_2RuO_4's magnetic ordering for L-Pbca structures at moderate pressures.

ACKNOWLEDGMENTS

B.R. and H.H. acknowledge support for this work from NSF Grant No. DMR-1726213, DOE Grant No. DE-SC0019441, and the Alfred P. Sloan Foundation. A.J.M. (partially) and Q.H. (fully) were supported by the Basic Energy Sciences Program of the U.S. Department of Energy under Grant No. DOE-SC-0012375. A.G. acknowledges partial support by the European Research Council (ERC-319286-QMAC). We are grateful to H. T. Dang for his contribution to some of the DMFT codes used in this work. This work was conducted using computational resources and services at the Brown University Center for Computation and Visualization, XSEDE, the Yeti HPC cluster at Columbia University, and the Flatiron Institute. The Flatiron Institute is a division of the Simons Foundation.

[1] E. Tsymbal and P. Dowben, Front. Phys. **1**, 32 (2013).
[2] J. P. F. LeBlanc, A. E. Antipov, F. Becca, I. W. Bulik, G. K.-L. Chan, C.-M. Chung, Y. Deng, M. Ferrero, T. M. Henderson, C. A. Jiménez-Hoyos, E. Kozik, X.-W. Liu, A. J. Millis, N. V. Prokof'ev, M. Qin, G. E. Scuseria, H. Shi, B. V. Svistunov, L. F. Tocchio, I. S. Tupitsyn, S. R. White, S. Zhang, B.-X. Zheng, Z. Zhu, and E. Gull (Simons Collaboration on the Many-Electron Problem), Phys. Rev. X **5**, 041041 (2015).
[3] B.-X. Zheng, C.-M. Chung, P. Corboz, G. Ehlers, M.-P. Qin, R. M. Noack, H. Shi, S. R. White, S. Zhang, and G. K.-L. Chan, Science **358**, 1155 (2017).
[4] M. Motta, D. M. Ceperley, G. K.-L. Chan, J. A. Gomez, E. Gull, S. Guo, C. A. Jiménez-Hoyos, T. N. Lan, J. Li, F. Ma, A. J. Millis, N. V. Prokof'ev, U. Ray, G. E. Scuseria, S. Sorella, E. M. Stoudenmire, Q. Sun, I. S. Tupitsyn, S. R. White, D. Zgid, and S. Zhang (Simons Collaboration on the Many-Electron Problem), Phys. Rev. X **7**, 031059 (2017).
[5] S. Zhang, J. Carlson, and J. E. Gubernatis, Phys. Rev. B **55**, 7464 (1997).
[6] S. Zhang, *Auxiliary-Field Quantum Monte Carlo for Correlated Electron Systems* (Springer-Verlag, Berlin, 2013), Chap. 15.
[7] A. Georges, G. Kotliar, W. Krauth, and M. J. Rozenberg, Rev. Mod. Phys. **68**, 13 (1996).
[8] Y. Maeno, H. Hashimoto, K. Yoshida, S. Nishizaki, T. Fujita, J. Bednorz, and F. Lichtenberg, Nature **372**, 532 (1994).
[9] S. Nakatsuji, S.-i. Ikeda, and Y. Maeno, J. Phys. Soc. Jpn. **66**, 1868 (1997).
[10] G. Cao, S. McCall, J. E. Crow, and R. P. Guertin, Phys. Rev. Lett. **78**, 1751 (1997).
[11] F. Nakamura, T. Goko, M. Ito, T. Fujita, S. Nakatsuji, H. Fukazawa, Y. Maeno, P. Alireza, D. Forsythe, and S. R. Julian, Phys. Rev. B **65**, 220402(R) (2002).

[12] P. Steffens, O. Friedt, P. Alireza, W. G. Marshall, W. Schmidt, F. Nakamura, S. Nakatsuji, Y. Maeno, R. Lengsdorf, M. M. Abd-Elmeguid, and M. Braden, Phys. Rev. B **72**, 094104 (2005).
[13] C. Sow, S. Yonezawa, S. Kitamura, T. Oka, K. Kuroki, F. Nakamura, and Y. Maeno, Science **358**, 1084 (2017).
[14] A. Georges, L. d. Medici, and J. Mravlje, Annu. Rev. Condens. Matter Phys. **4**, 137 (2013).
[15] M. Braden, G. André, S. Nakatsuji, and Y. Maeno, Phys. Rev. B **58**, 847 (1998).
[16] C. S. Alexander, G. Cao, V. Dobrosavljevic, S. McCall, J. E. Crow, E. Lochner, and R. P. Guertin, Phys. Rev. B **60**, R8422 (1999).
[17] O. Friedt, M. Braden, G. André, P. Adelmann, S. Nakatsuji, and Y. Maeno, Phys. Rev. B **63**, 174432 (2001).
[18] F. Nakamura, J. Phys. Soc. Jpn. **76**, 96 (2007).
[19] V. I. Anisimov, I. A. Nekrasov, D. E. Kondakov, T. M. Rice, and M. Sigrist, Eur. Phys. J. B **25**, 191 (2002).
[20] J. H. Jung, Z. Fang, J. P. He, Y. Kaneko, Y. Okimoto, and Y. Tokura, Phys. Rev. Lett. **91**, 056403 (2003).
[21] A. Liebsch and H. Ishida, Phys. Rev. Lett. **98**, 216403 (2007).
[22] E. Gorelov, M. Karolak, T. O. Wehling, F. Lechermann, A. I. Lichtenstein, and E. Pavarini, Phys. Rev. Lett. **104**, 226401 (2010).
[23] G. Zhang and E. Pavarini, Phys. Rev. B **95**, 075145 (2017).
[24] Q. Han and A. Millis, Phys. Rev. Lett. **121**, 067601 (2018).
[25] G. Kresse and J. Hafner, Phys. Rev. B **47**, 558 (1993).
[26] G. Kresse and J. Furthmüller, Comput. Mater. Sci. **6**, 15 (1996).
[27] G. Kresse and J. Furthmüller, Phys. Rev. B **54**, 11169 (1996).
[28] G. Kresse and D. Joubert, Phys. Rev. B **59**, 1758 (1999).
[29] N. Marzari and D. Vanderbilt, Phys. Rev. B **56**, 12847 (1997).
[30] I. Souza, N. Marzari, and D. Vanderbilt, Phys. Rev. B **65**, 035109 (2001).
[31] H. T. Dang and A. J. Millis, Phys. Rev. B **87**, 155127 (2013).
[32] H. T. Dang, J. Mravlje, A. Georges, and A. J. Millis, Phys. Rev. B **91**, 195149 (2015).
[33] Q. Han, H. T. Dang, and A. J. Millis, Phys. Rev. B **93**, 155103 (2016).
[34] J. Mravlje, M. Aichhorn, T. Miyake, K. Haule, G. Kotliar, and A. Georges, Phys. Rev. Lett. **106**, 096401 (2011).
[35] D. Sutter, C. G. Fatuzzo, S. Moser, M. Kim, R. Fittipaldi, A. Vecchione, V. Granata, Y. Sassa, F. Cossalter, G. Gatti, M. Grioni, H. M. Ronnow, N. C. Plumb, C. E. Matt, M. Shi, M. Hoesch, T. K. Kim, T.-R. Chang, H.-T. Jeng, C. Jozwiak, A. Bostwick, E. Rotenberg, A. Georges, T. Neupert, and J. Chang, Nature Commun. **8**, 15176 (2017).
[36] H. Hao, B. M. Rubenstein, and H. Shi, Phys. Rev. B **99**, 235142 (2019).
[37] J. Kanamori, Prog. Theor. Phys. **30**, 275 (1963).
[38] See Supplemental Material at http://link.aps.org/supplemental/10.1103/PhysRevB.101.235110 for further details about the one-body Hamiltonian matrix of Ca_2RuO_4 intrasite and intersite interactions, technical details in auxiliary field quantum Monte Carlo and dynamical mean field theory calculations.
[39] M. Qin, H. Shi, and S. Zhang, Phys. Rev. B **94**, 235119 (2016).
[40] O. Parcollet, M. Ferrero, T. Ayral, H. Hafermann, I. Krivenko, L. Messio, and P. Seth, Comput. Phys. Commun. **196**, 398 (2015).
[41] P. Seth, I. Krivenko, M. Ferrero, and O. Parcollet, Comput. Phys. Commun. **200**, 274 (2016).
[42] E. Eidelstein, E. Gull, and G. Cohen, Phys. Rev. Lett. **124**, 206405 (2020).
[43] P. Lebre Alireza, S. Barakat, A.-M. Cumberlidge, G. Lonzarich, F. Nakamura, and Y. Maeno, J. Phys. Soc. Jpn. **76**, 216 (2007).
[44] S. Nakatsuji and Y. Maeno, Phys. Rev. Lett. **84**, 2666 (2000).